Optimization of flow diverters for cerebral aneurysms

Hitomi Anzai[a], Makoto Ohta[a], Jean-Luc Falcone[b], Bastien Chopard[b,*]

[a] *Tohoku University, Japan*
[b] *University of Geneva, Switzerland*

ABSTRACT

A modern technique to treat cerebral aneurysms is to insert a flow diverter in the parent artery. In order to produce an optimal design of such devices, we consider a methodology combining simulated annealing optimization and lattice Boltzmann simulations. Our results surpass, in terms of stent efficiency, those obtained in the recent literature with an other optimization method. Although our approach is still in 2D, it demonstrates the potential of the method. We give some hint on how the 3D cases can be investigated.

© 2012 Elsevier B.V. All rights reserved.

1. Introduction

Cardiovascular disease, including heart disease and cerebral vascular disease, is one of the greatest causes of death in developed countries. Cerebral aneurysm is a vascular disorder that distends the vessel wall (see Fig. 1). In most cases, subarachnoid hemorrhage from a ruptured intracranial aneurysm impairs the quality of life of patients. In recent years endovascular treatments have attracted much attention due to their minimal invasiveness and good prognosis of patients.

The aim of endovascular treatments is to reduce the blood flow in an aneurysm by the placement of a device in the aneurysm (coil) and/or in the parent artery (stent or flow diverter). As a result of the flow reduction in the aneurysms, embolization by clot formation is expected to occur in the cavity, thus healing the aneurysm by its occlusion.

Aenis et al. reported that a stent has a capability of reduction of the flow in an aneurysm [1] and the reduction may lead to repair. Subsequent studies of sole stenting to reduce the flow more as a "flow diverter" rather than a "support for coiling" have been performed [2,3]. These studies have revealed that the effect of a stent on flow is not only dependent on porosity but also on the design of a stent.

In order to find a stent design that reduces the flow in aneurysm effectively, Srinivas et al. [4] applied an optimization procedure to determine the best stent structure across the neck of a 2D aneurysm, by sampling numerical simulations with different designs. This study shows that a better flow reduction is achieved when stent struts are concentrated at the edge of aneurysm neck rather than uniformly along the orifice.

Nakayama et al. investigated the size of strut with 80% porosity using a multi-objective genetic algorithm and kriging [5]. Finite volume method (FVM) was used and mesh generation turned out to be a delicate issue. Indeed all stent designs required handmade mesh generation, making it almost impossible to find out the best design with an automatic process. On the other hand, the Lattice Boltzmann (LB) method (see for instance [6]) uses a Cartesian mesh which can accommodate any stent design without having to generate the mesh manually. LB is a class of CFD methods for fluid simulations which represents a fluid as a set of fictitious particles moving and colliding on a regular lattice. It has been successfully used for many complex flow simulations. Hirabayashi et al. [7] applied the LB method to show the relationship between stent position and flow in aneurysm, thus illustrating the possibility of using LB simulation to study the effect of the stent fine scale details on blood circulation in cerebral aneurysms. In particular, when using stents with coarse struts, the flow reduction in aneurysm depends heavily on the stent position across the neck. Kim et al. [8] analyzed the shape of the strut cross section and concluded that rectangular struts reduce the flow more effectively than triangular or circular ones.

* Corresponding author. Tel.: +41 22 379 0219.
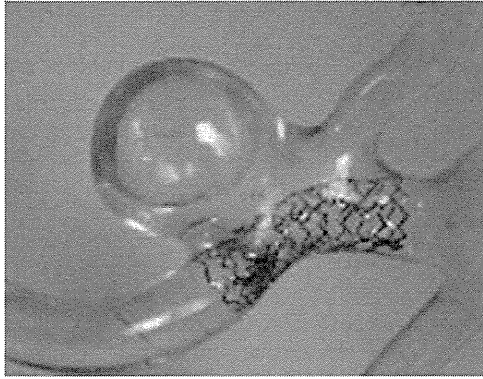 *E-mail address:* Bastien.Chopard@unige.ch (B. Chopard).

Fig. 1. An in vitro model of a cerebral aneurysm with a stent.

Fig. 2. Geometry of an ideal sidewall 2D aneurysm.
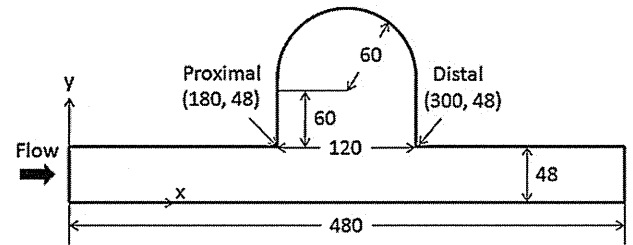
In this paper, we consider the possibility to use LB bloodflow simulations in combination with an optimization algorithm that can explore the design space of stents (or flow diverters), in a fully automated way. Optimization method may require a huge number of flow simulations to determine the best stent geometry. In the simulated annealing optimization that we consider here, simulations have to be done one after another. The advantages of the LB method in this respect is that it can be massively parallelized on huge scale computers, thus reducing significantly the wall clock time of each flow simulation.

Simulated annealing (SA) is a classical probabilistic metaheuristics applicable to hard optimization problems and especially to combinatorial optimization [9–11]. It can be shown to converge in probability to a global optimal, if the parameters are well chosen. In practice, SA searches effectively through a large solution set for good approximations of a global minimum. In our case, the objective function is defined as the average velocity norm inside the aneurysm. From one run to the next, the stent design is slightly modified, while preserving a prescribed porosity. If the new design produces a slower flow in the aneurysms cavity, the change is accepted. If not, the change is accepted with some probability, which depends on the current so-called "temperature", a parameter which guide the optimization process.

This paper focuses on a 2D ideal sidewall aneurysm in view of a feasibility study. In a forthcoming study, we shall report on the 3D, more realistic case.

2. Method

2.1. Lattice Boltzmann simulations

The Lattice Boltzmann (LB) method is an acknowledged alternative to standard computational fluid dynamics (CFD) techniques to solve the Navier–Stokes equations and other partial differential equations. It is described in several textbooks or review papers (see for instance [6,12,13]).

The LB method for hydrodynamics is a mesoscopic approach in which a fluid is described in terms of density distributions of idealized fluid particles moving and colliding on a regular lattice. These fluid particles can only take a finite number of possible velocities such that, in one time step of the dynamics, particles move from one lattice site to another.

Advantages of the LB method over more traditional numerical schemes are its simplicity, its flexibility to describe complex flows and its local nature (no need to solve a Poisson equation). LB solvers can be parallelized very naturally and scale well up to thousands of processors.

Here we perform 2D flow simulations using the standard D2Q9 lattice and the so-called single-time, BGK relaxation method [6,12]

The problem we consider corresponds to the model of Srinivas et al. [4], illustrated in Fig. 2. The parent artery has length $L = 40$ mm and diameter 4 mm. The aneurysm cavity has a depth and a neck of 10 mm. The spatial discretization is chosen as $\Delta r = 1/12$ mm, so that the full simulation fits in a lattice with 480×168 sites. The stent is modeled as a set of struts along the neck of the aneurysms. Each strut occupies one lattice site.

In order to impose no-slip boundary conditions on the walls of the vessel and the aneurysm, as well as on the lattice points that correspond to the stent struts, we use the well known bounce-back rule: the fluid particles bounce from were they came when hitting a no-slip lattice site (the velocity direction is reversed while the magnitude remains constant). The inlet boundary is defined as a velocity boundary condition, a steady parabolic profile with maximum velocity $U = 0.15$, in lattice units. On the outlet, a pressure boundary is imposed. In order to achieve a Reynolds number of 300, the kinetic viscosity is chosen as $v = UL/Re = 0.024$, giving a relaxation time $\tau = (6v + 1)/2 = 0.57$.

LB simulations are inherently time-dependent. The steady state is reached when the flow does not change anymore. Here, the steady state is assumed to be attained if the standard deviation of the average kinetic energy over the last 5000 time steps is less than 1.5×10^{-6}.

In this study, the open source software Palabos [14], version 0.7, which provides a flexible, highly parallelized and publicly available environment for the LB method, was used for the computational fluid dynamics (CFD) simulations. The optimization program developed in this study was run with 1, 15 and 20 CPUs.

2.2. Optimization method

The algorithm we used for stent shape optimization is the simulated annealing (SA) method. The steps of the algorithm are indicated in Fig. 3. In short, an initial stent geometry S_{init} is considered at the beginning of the process. The quality of this stent is evaluated through CFD simulations based on the LB method, by computing the average velocity V in the aneurysm

$$V = \frac{\sum_{\mathbf{r}} \sqrt{u_x^2(r) + u_y^2(t)}}{N} \tag{1}$$

where the summation is carried out over all N lattice sites $\mathbf{r}$ inside the aneurysm cavity.

The average velocity V given by (1) is taken as the objective (or fitness) function of the problem. The goal is to find a stent design that minimizes it.

Note that other fitness functions can be considered. However, the property that an optimal stent should verify is still an open question. Velocity reduction in the cavity is a simple metric which can be used to demonstrate the potential of our approach and that allows for a comparison with the results found in [4].

As suggested in Fig. 3, the SA method proceeds by applying iteratively random modifications to the current stent geometry, until an optimal design is reached. The specificity of SA is to accept with some probability modifications that degrade the efficiency of the
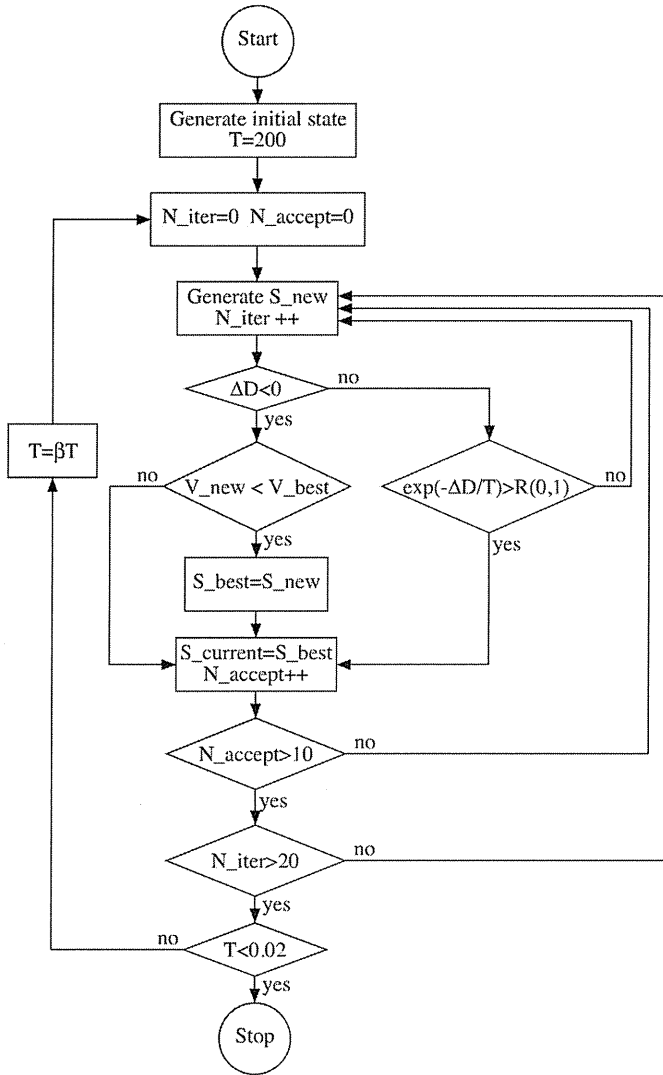
Fig. 3. Flow diagram of the simulated annealing optimization process, according to [15].

stent. Let us call S_{new} a new stent geometry obtained from the current geometry $S_{current}$, through a small modification of its structure. In practice, this modification is obtained by exchanging randomly a lattice strut node with a fluid node, along the line defined by the

aneurysm neck. In this way, the modification does not change the porosity of the stent.

The improvement of S_{new} over $S_{current}$ is computed as the variation ΔD of the fitness function

$$\Delta D = V_{new} - V_{current} \tag{2}$$

The modification is accepted if

$$\exp\left(\frac{-\Delta D}{T}\right) > R[0, 1] \tag{3}$$

where $R[0, 1]$ is a random number between 0 and 1 and T is the current "temperature" of the SA process. At the beginning, the temperature is high (here we start with $T = 200$) and changes are often accepted even though they may degrade the quality of the stent. In this phase of the optimization, the exploration of the search space is dominant. However, when at a given temperature level k, no more improvement are observed on average, the temperature is decreased according to a prescribed temperature schedule. Here we chose $T_{k+1} = \beta T_k$ with $\beta = 0.9$. The optimization process is stopped when $T = 0.02$ is reached.

All along the optimization, the best geometry S_{best} seen so far is remembered. Whenever $V_{new} < V_{best}$, S_{new} becomes S_{best}. At the end of the process, S_{best} is given as the optimal solution.

3. Results

In order to show the independence of the optimal stent on the initial condition of the SA search, four initial combinations for struts positions were considered, as depicted in Fig. 4. They are referred to as cases A, B, C and D. In principle, if the optimization process is not blocked in a local minimum, all these initial configurations should eventually evolved towards the same global optimum. We chose a porosity of 80% (which is kept constant during the optimization procedure) to better compare our result with those reported in [4]. Note however that this porosity is higher than that of current flow diverters.

To express the results of our optimization in a dimensionless form, we use the flow reduction index R_f defined as

$$R_f = \frac{V_{w/o} - V_{current}}{V_{w/o}} \tag{4}$$

where $V_{w/o}$ is the average velocity, computed from Eq. (1) without stent.

Fig. 5 shows the flow pattern without stent and with each of the four initial stents. The flow enters the aneurysm on the proximal side of the neck, and then goes out on the distal side. Secondary flow occurs inside the aneurysm. The initial stent B leads to a fast inflow
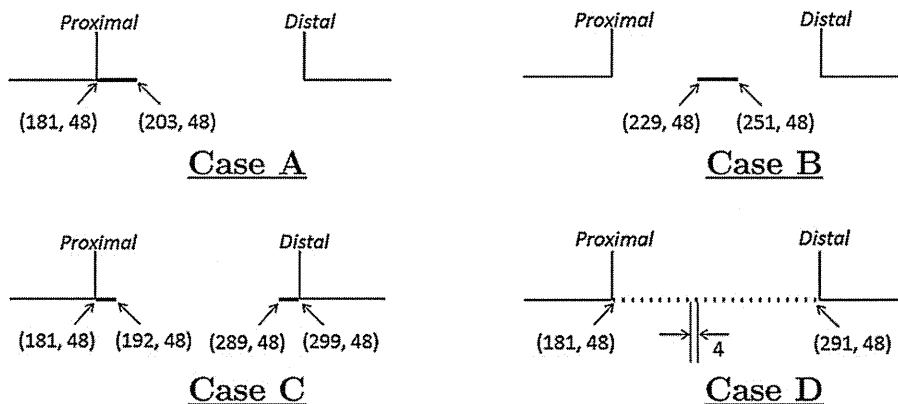

Fig. 4. The four initial stent geometries used for the optimization process. Only the aneurysm neck is shown here, between the proximal and distal points. The stent struts are indicated in bold.
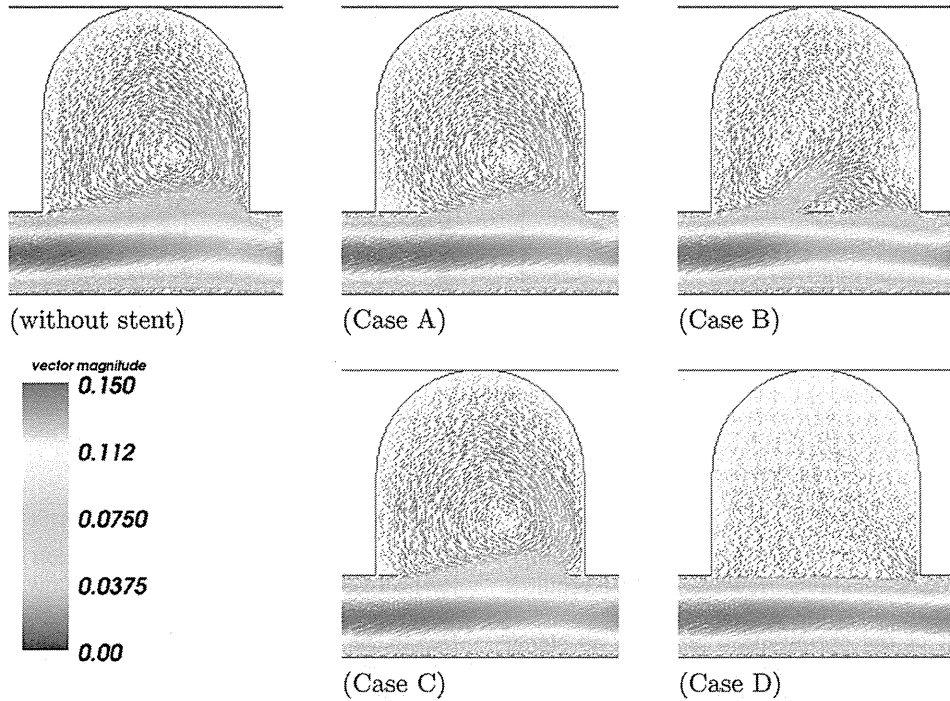
Fig. 5. Flow pattern before stent optimization. From left to right, top to bottom: situation without stent, then cases A, B, C and D.
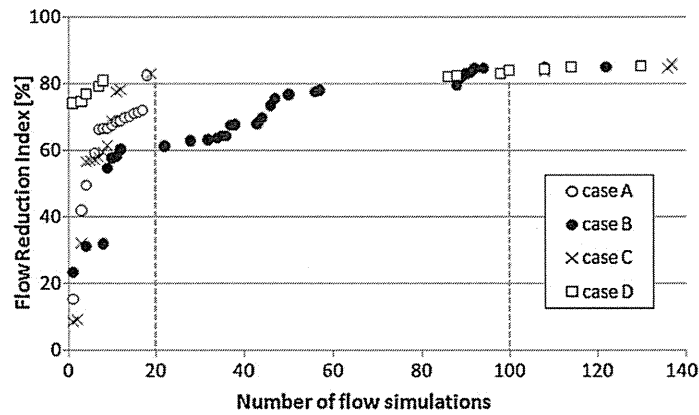

Fig. 6. Evolution of the flow reduction index as a function of the simulated annealing iteration, for the four initial stent geometries.

into the aneurysm. Initial stents A and C narrow the orifice of the aneurysm (see Fig. 4), thus reducing this inflow. Initial stent D has a uniform distribution of struts and shows a good flow reduction of $R_f = 74\%$ even before the optimization process.

Fig. 6 shows the improvement of flow reduction on each stent shape during the optimization process. The horizontal axis represents the number of flow simulations, which counts both accepted and unaccepted stent modifications. The data points shown in this
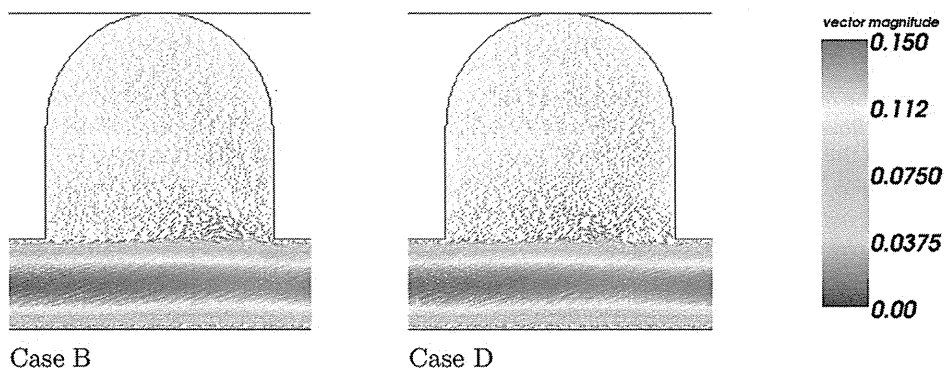

Fig. 7. Flow pattern (velocity vector) obtained with stent geometry B (left) and D (right), after optimization.

Fig. 8. Strut distribution along the aneurysm neck for the four initial stents, after the optimization process.
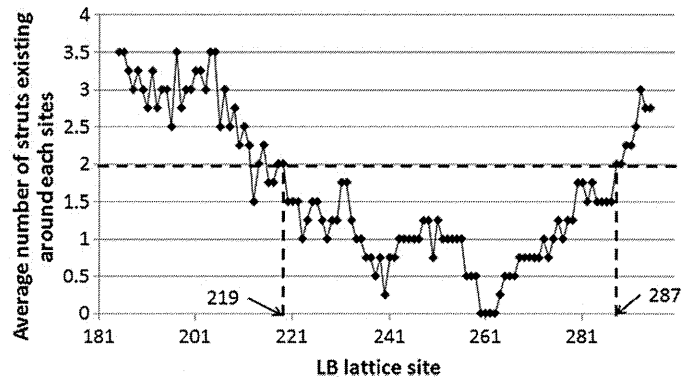

Fig. 9. Number of struts in an interval around each lattice node. The average is performed over the optimized geometries A, B, C and D.

figure only correspond to iterations at which an improvement of R_f has been accepted and R_f has shown the best score. In this figure, the first 140 flow simulations are shown, however about 1800 of them are performed for each case. We observe a rapid improvement of the flow reduction within the first 100 flow simulations followed by a saturation phase. Stents A, C and D obtain 80% of flow reduction within 20 flow simulations. However, stent B requires 100 simulations to reach $R_f > 80\%$.

After the execution of the optimization program, all stents evolve to the new geometry shown in Fig. 8, corresponding to the flow pattern illustrated in Fig. 7, for cases B and D. In Fig. 8, black squares indicate the struts. Struts are distributed over the neck, with high density at both the proximal and distal ends. A low density region appears in the center. Flow reduction R_f in the aneurysm reaches 89% in all cases. The highest reduction is obtained in case B and the lowest one is obtained in case D. Table 1 summarizes the flow reduction R_f observed before and after stent optimization for all cases.

The optimized stents A, B, C and D are not all exactly the same. This is likely due to premature convergence of the SA process, or to the existence of several optimal geometries. However, in terms of stent design, none of the design in Fig. 8 is satisfactory, due to the irregularity of strut distribution. A *regularized* stent can however be devised, in order to produce a consensus of the four geometries and enforce a more regular spacing of the struts.

The regularized stent can be thought of an average of the four optimized configuration. It is built as follows. From Fig. 8 one sees that all four stents have typically three regions with different average porosity: the proximal, central and distal ones. Fig. 9 shows the average, over the four stents, of the number of struts along the neck located in a sliding window containing 9 lattice sites (about $\ell = 0.75$ mm). The limits of the three regions are defined as the points where this number crosses the horizontal line at ordinate 2, the value 2 being chosen arbitrarily. As illustrated in Fig. 10, the three regions obtained in this way are of size $39\Delta r$, $68\Delta r$ and $12\Delta r$, respectively. In addition, the average porosity in each of these regions are found to be 66.7%, 91.2% and 66.7%. The porosity in these three regions can be achieved with 13, 6 and 4 struts, respectively. One can easily check that this choice produces an average porosity of 80% across the aneurysm neck, as required.

The reduction index R_f for the regularized stent shown in Fig. 10 can then be obtained by a LB flow simulation. We find $R_f = 88.6\%$, which is less good than any of the optimal cases A, B, C and D, but still a quite reasonable efficiency.

4. Discussion

This paper describes the combination of simulated annealing (SA) with lattice Boltzmann (LB) bloodflow calculations to discover the optimal stent design that best suit a given aneurysm geometry. Due to the simple Cartesian grid used in LB simulation, this combined approach is appropriate for a fully automated search process, as no manual fine tuning of the computational mesh around the stent struts is required each time a new stent design is tested.

LB simulations can be easily parallelized, and this is done automatically with the Palabos software. Therefore it is suited for large-scale parallel computation. In this study, for comparison purposes, the optimization program is performed for a 2D ideal aneurysm with both serial and parallel runs. The optimal stent design is obtained in 48 h with serial computing, whereas it takes 9 and 5 h with 10 and 20 CPUs, respectively. In principle, many more computing cores can be considered. Palabos has been shown to scale very well up to thousands of cores. Such a large scale parallelization will be needed when optimizing 3D geometries.

Theoretically, the SA method is able to find the global optimum if the initial temperature and cooling schedule are well chosen. Here we have considered a set of parameters that lead to a rather fast convergence but, very likely, a convergence to local optima. This is illustrated by the difference in the solution of the four initial stent geometries. However, the flow reduction index R_f, is quite similar between the four cases. It reaches 80% within the first 100 iterations and then stay more or less constant until the end of the program. The best stent we have obtained achieves 89% of velocity reduction.

The dependence of the above results on the mesh size is an important issue. In our case, we have checked that doubling the mesh resolution (i.e representing the struts by a 2 × 2 pixels instead of 1 × 1) modifies the velocity reduction obtained with the optimal stent by less than 1%.

It is interesting to compare this result with another optimization approach using the same aneurysm. Srinivas et al. [4] obtained about 76% of velocity reduction with an optimized stent, whose porosity is 80% and consisting of five wide struts, instead of the 23 thin ones, we obtain here. The CPU time reported by Srinivas et al. is from 2 min to 60 min for one geometry, depending upon the case considered and the type of computer used. The method requires

Table 1

Flow reduction R_f for geometries A, B, C and D, before and after optimization.

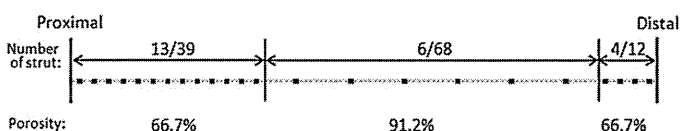|	Case A [%]	Case B [%]	Case C [%]	Case D [%]
Initial state	15.3	23.3	8.5	74.3
Optimized state	89.4	89.8	89.5	89.2

Fig. 10. The regularized stent, obtained as a regular consensus of optimal stents A, B, C and D.
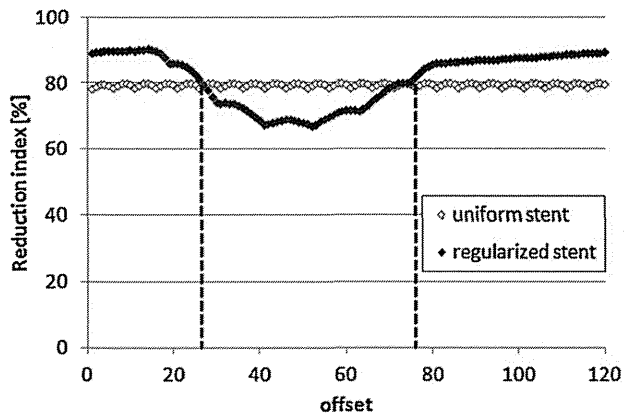
Fig. 11. Variation of the flow reduction obtained with the optimal regularized stent as a function of its positioning along the neck. This variation is compared to the flow reduction achieved with a uniform stent with the same porosity.

the calculation of the flows patterns for 60 different geometries. Mesh and geometry are constructed by an operator and the operation time should be considered. On a personal computer, one can thus assume that the CPU time is around 60 × 60 min, i.e. 60 h. This more than the CPU time of our approach on a personal computer (48 h), and it produces a less optimal stent than ours.

All of the optimized stents we have generated have a non-uniform distribution of struts. They are dense at both proximal and distal ends, with a sparse region in the middle. The dense part at the proximal end is longer than the distal one. This feature is consistent with the inflow and outflow patterns observed in aneurysm geometry such as the one we consider here. Anzai et al. [16] have reported that struts placed where the flow enters the aneurysm decrease the flow more effectively than struts placed where the flow leaves the cavity. This suggests that the optimized stent will become dense at the inflow zone even in realistic 3D geometry.

A non-uniform stent raises the question of the sensitivity of the flow reduction index on the stent position along the neck. As shown in Fig. 11, the regularized stent provides a higher R_f than a uniform one within a tolerance of two to three millimeters from its optimal position. However, when the high porosity part of the regularized stent is situated at proximal end of the neck, R_f becomes lower than with an uniform stent with 80% of porosity.

Fig. 6 shows the variation of the number of SA iterations needed to converge to the optimal state, from different initial conditions. This variation suggests that starting with an initial stent geometry close to the optimal one will significantly save computational time. This might be important for 3D optimizations.

In this study, the flow is steady and Newtonian. This can be easily changed by adapting the boundary conditions of the flow solver and to turn on a non-Newtonian rheology in the LB solver (see for instance [17,18]). Of course, time-dependent flow simulations are expected to be more costly than steady ones. However, since the LB method is inherently time-dependent, this will not add so much extra computational time to the full optimization process. In the near future, we plan simulations with pulsatile flows to determine how the optimal stent structure changes with respect to the steady case.

Of course, the present approach should be extended to 3D to be of practical importance. There are several issues to be solved in relation to the vast increase of the search space and computational load. The 3D extension is part of an ongoing study, the European FP7 VPH project THROMBUS. In addition to computational time, the challenge of the 3D case is the stent representation in the computer and the definition of the elementary changes required by the SA algorithm.

We shall first consider the ideal side-wall aneurysm, then realistic aneurysm obtained from medical imaging with the purpose to achieve tailor-made medicine.

Several approaches can be considered to address the 3D problem. We can use the same method as in the 2D case and interpret the resulting spatial distribution of struts as an indication of the zones with optimal porosity. Or we can consider only geometry modifications that guarantee the continuity of the wires making up the stent. Finally, if the stent geometry can be described by a mathematical parametrization, the SA can be used to find the optimal values of these parameters.

Note finally that a proper choice of objective function is required to make meaningful predictions on stent performance. However, it is still unknown which quantities are critical for the growth and the rupture of an aneurysm, or are needed to induce thrombosis in the cavity. Thus, at the present time, we considered the single-objective optimization specified by the minimization of the average velocity inside the aneurysm. But our approach can be equally well applied with any objective function, such as the oscillatory shear index (OSI) [19], flow complexity [20], gradient oscillatory number (GON) [21], and even multi-objective problems.

5. Conclusions

Stent optimization is a step toward an era of tailor-made medicine for each individual.

In this paper, stent design based on the combination of Lattice Boltzmann flow simulations and Simulated Annealing optimization was developed for a 2D ideal aneurysm geometry. Although only 3D stent optimization is relevant for medical applications, the 2D case presented here serves as a feasibility study. Our results on the full 3D problem are still in an early stage and will be reported in the future.

Our results can be summarized as follows. After execution of the optimization process with four initial stent geometries, all of them were reshaped through a succession of elementary modification that, eventually, produce over 89% of flow reduction inside the aneurysm cavity. As a next step, we proposed a *regularized* stent geometries which can be thought of as a design average of the four optimized stents. This consensus stent is made of three sections, alternating dense and sparse porosity. This stent produces 88.6% of flow reduction, in good agreement with the reduction reached by the four optimal stents.

Except from initial stent condition B, a flow reduction of 80% is obtained within the first 20 iterations of the simulated annealing process. Case B required over 80 modifications until the flow reduction reaches that level. This difference of effort to obtain a good stent efficiency suggests the importance of choosing an appropriate initial state.

The present approach can be fully automated and run on large scale parallel computers. It achieves a significantly better stent design than the one obtained in a recent study by Srinivas et al. [4], with less CPU requirements on a serial machine.

References

[1] M. Aenis, et al., Modeling of flow in a straight stented and nonstented side wall aneurysm model, J. Biomech. Eng.-Trans. ASME 119 (2) (1997) 206–212.

[2] S. Appanaboyina, et al., Simulation of intracranial aneurysm stenting: Techniques and challenges, Comput. Methods Appl. Mech. Eng. 198 (45–46) (2009) 3567–3582.

[3] L. Augsburger, et al., Effect of flow diverter porosity on intraaneurysmal blood flow, Clin. Neuroradiol.[[nl]]Klinische Neuroradiologie 19 (3) (2009) 204–214.

[4] K. Srinivas, et al., Two-dimensional optimization of a stent for an aneurysm, J. Med. Dev. Trans. ASME 4 (2) (2010) 021003.

[5] T. Nakayama, et al., Development of stent strut pattern for cerebral aneurysm, in: Proceedings of the 3rd ASME 2010 Joint US-European Fluids Engineering Summer Meeting and 8th International Conference on Nanochannels, Microchannels, and Minichannels:FEDSM/ICNMM, 2010, p. 30592.

[6] S. Succi, The Lattice Boltzmann Equation, For Fluid Dynamics and Beyond, Oxford University Press, 2001.

[7] M. Hirabayashi, M. Ohta, D.A. Rufenacht, B. Chopard, Characterization of flow reduction in an aneurysm due to a porous stent, Phys. Rev. E 68 (2003) 021918.

[8] Y. Kim, X. Xu, J. Lee, The effect of stent porosity and strut shape on saccular aneurysm and its numerical analysis with lattice Boltzmann method, A. Biomed. Eng. 38 (7) (2010) 2274–2292.

[9] S. Kirkpatrick, Optimization by simulated annealing—quantitative studies, J. Stat. Phys. 34 (1984) 5–6.

[10] D. Johnson, et al., Optimization by simulated annealing—an experimental evaluation, Oper. Res. (1991).

[11] D. Bertsimas, J. Tsitsiklis, Simulated annealing, Stat. Sci. 8 (1) (1993) 10–15.

[12] B. Chopard, P. Luthi, A. Masselot, A. Dupuis, Cellular automata and lattice Boltzmann techniques: an approach to model and simulate complex systems, Adv. Complex Syst. 5 (2) (2002) 103–246, http://cui.unige.ch/~chopard/FTP/CA/acs.pdf.

[13] C. Aidun, J. Clausen, Lattice-Boltzmann method for complex flows, Ann. Rev. Fluid Mech. 42 (1) (2010) 439–472.

[14] http://http://www.palabos.org/.

[15] P.J.M. Laarhoven, E.H.L. Aarts (Eds.), Simulated annealing: theory and applications, Kluwer Academic Publishers, Norwell, MA, USA, 1987.

[16] H. Anzai, et al., The effect of 3d visualization on optimal design of strut position of intracranial stent, in: Proceedings of the 3rd ASME 2010 Joint US-European Fluids Engineering Summer Meeting and 8th International Conference on Nanochannels, Microchannels, and Minichannels:FEDSM/ICNMM, 2010, p. 30591.

[17] B. Chopard, R. Ouared, D.A. Ruefenacht, H. Yilmaz, Lattice Boltzmann modeling of thrombosis in giant aneurysms, Int. J. Mod. Phys. C 18 (2007) 712–721.

[18] O. Malaspinas, G. Courbebaisse, M. Deville, Simulation of generalized newtonian fluids with the lattice Boltzmann method, Int. J. Mod. Phys. C 18 (2007) 1939.

[19] D. Ku, D. Giddens, C. Zarins, S. Glagov, Pulsatile flow and atherosclerosis in the human carotid bifurcation—positive correlation between plaque location and low and oscillating shear-stress, Arteriosclerosis 5 (3) (1985) 293–302.

[20] J.R. Cebral, F. Mut, J. Weir, C.M. Putman, Association of hemodynamic characteristics and cerebral aneurysm rupture, Am. J. Neuroradiol. 32 (2) (2011) 264–270.

[21] Y. Shimogonya, T. Ishikawa, Y. Imai, N. Matsuki, T. Yamaguchi, Can temporal fluctuation in spatial wall shear stress gradient initiate a cerebral aneurysm? A proposed novel hemodynamic index the gradient oscillatory number (GON), J. Biomech. 42 (4) (2009) 550–554.

Hitomi Anzai is a PhD student, Graduate School of Engineering, Tohoku University. She has graduated in School of Engineering, Tohoku University (2005–2009), and then entered Graduate School of Engineering, Tohoku University (2009–present). She is a research fellow of the Japan Society for the Promotion of Science for Young Scientists. Her research field is computed fluid dynamics on/in intracranial aneurysm.
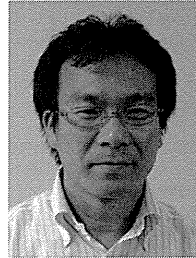
Makoto Ohta received a PhD in Biopolymers from Department of Polymer Chemistry, Kyoto University (2001). He then worked in Institute for Frontier Medical Sciences, Kyoto University (2001) and spent several years at the University Hospital of Geneva as a research fellow and post-doctoral position (2001–2004). He is now associate professor at Institute of Fluid Science, Tohoku University (2005–present). His research topics are design development of intracranial stent based on blood flow dynamics, and development of biomodelling for evaluation of medical devices. He published over 50 publication based on the biomechanics and biomaterial fields.

Dr. Jean-Luc Falcone is a researcher in the University of Geneva. He is a biologist with a strong background in computational science and data-mining methods for life sciences. Since June 2010, he has been working for the lemanic center CADMOS as High Performance Computing analyst.
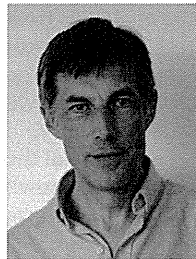
Bastien Chopard received a PhD in theoretical physics from the University of Geneva (1988). He then spent two years in the Laboratory for Computer Science, at the Massachusetts Institute of Technology and one year at the Center for High Performance Computing in the Research Center in Jülich, Germany. He is now professor at the Department of Computer Sciences of the University of Geneva. His research interests concern the modeling and simulation of complex systems on parallel computers. A large part of his work concerns the field of cellular automata, lattice gas and lattice Boltzmann techniques. Numerical simulation of biomedical applications is an important part of his current research activities. He published about 200 papers and is co-author of a textbook on Cellular Automata modeling of Physical systems (Cambridge University Press, 1998).

Lab on a Chip

PAPER

Separation of cancer cells from a red blood cell suspension using inertial force

Tatsuya Tanaka,[a] Takuji Ishikawa,*[a] Keiko Numayama-Tsuruta,[b] Yohsuke Imai,[a] Hironori Ueno,[c] Noriaki Matsuki[d] and Takami Yamaguchi[b]

The circulating tumor cell (CTC) test has recently become popular for evaluating prognosis and treatment efficacy in cancer patients. The accuracy of the test is strongly dependent on the precision of the cancer cell separation. In this study, we developed a multistage microfluidic device to separate cancer cells from a red blood cell (RBC) suspension using inertial migration forces. The device was able to effectively remove RBCs up to the 1% hematocrit (Hct) condition with a throughput of 565 µL min^{-1}. The collection efficiency of cancer cells from a RBC suspension was about 85%, and the enrichment of cancer cells was about 120-fold. Further improvements can be easily achieved by parallelizing the device. These results illustrate that the separation of cancer cells from RBCs is possible using only inertial migration forces, thus paving the way for the development of a novel microfluidic device for future CTC tests.

1. Introduction

Cancer remains one of the most deadly diseases in many developed countries. Because 90% of all cancer-related deaths occur due to cancer metastasis,[30] it is crucial to accurately detect the metastasis or recurrence of cancer at an early stage. Recently, the circulating tumor cell (CTC) test has become popular for evaluating prognosis and treatment efficacy in cancer patients.[4,8,9] In such tests, the condition of a patient is evaluated by counting the number of cancer cells in a peripheral blood sample; thus, the identification or separation of cancer cells from other blood cells is necessary. The accuracy of the CTC test is strongly dependent on the precision of cell identification or separation. Because conventional methods require several biochemical techniques for identification, they have serious drawbacks, such as high costs, long process times, and complex procedures.

Several techniques have been developed for separating cells, such as fluorescence-activated cell sorting (FACS), magnetic sorting, and dielectrophoresis.[11,24] Because these separation techniques require that the cells be labeled, they have problems of high cost, a complex preparation procedure, and the need for a large space to house the separation apparatus.

With the recent rapid progress of micro-fabricating technologies, passive microfluidic devices, which use only hydrodynamic forces for separation, have received much attention because of their favorable properties, such as low cost, simple procedure, and the small amount of space needed to house the apparatus. Separation based on the inertial migration of particles is one of these techniques,[7] which is typically applied to the separation of rigid spheres with different sizes.[18] Because the throughput of this separation method is very high, we think it may be suitable for CTC tests dealing with large numbers of cells.

Recently, some groups have succeeded in detecting or separating different cell types using an inertial migration effect. Kuntaegowdanahalli et al.[14] developed a five-loop Archimedean spiral microchannel and separated SH-SY5Y neuroblastoma cells (~15 µm in diameter) from C6 rat glioma cells (~6 µm in diameter).[2] They were able to perform the separation using a combination of inertial migration force and the Dean force generated by the centrifugal effect. Hur et al. demonstrated three-dimensional focusing of cells through channels using inertial migration forces.[12] Because this alignment could prevent overlapping and out-of-focus cells, their device allowed RBCs and leukocytes to be counted using image analysis. Carlo and coworkers applied the inertial migration effect to isolate platelets or bacteria from other blood cells in a diluted suspension, and succeeded in enriching the relative number of platelets and bacteria.[5,6,17]

Most recently, Bhagat et al. developed a microfluidic device that utilizes a pinched effect and inertial migration effect for separating cancer cells from a diluted whole blood sample.[3] It consisted of a cell-focusing region and a rare-cell pinching region. In the cell-focusing region, all cells migrated and aligned near the sidewalls due to inertial migration forces. The rare-cell pinching region had a geometry that contained contraction-expansion

[a] Dept. Bioengineering and Robotics, Graduate School of Engineering, Tohoku University, 6-6-01 Aoba, Aramaki, Aoba-ku, Sendai, 980-8579, Japan. E-mail: ishikawa@pfsl.mech.tohoku.ac.jp; Fax: +81-22-795-6959; Tel: +81-22-795-4009
[b] Dept. Biomedical Engineering, Graduate School of Biomedical Engineering, Tohoku University, 6-6-01 Aoba, Aramaki, Aoba-ku, Sendai 980-8579, Japan
[c] International Advanced Research and Education Organization, Tohoku University, 6-6-01 Aoba, Aramaki, Aoba-ku, Sendai, 980-8579, Japan
[d] Dept. Biomedical Engineering, Graduate School of Engineering, Okayama University of Science, Ridai-cho, Okayama 700-0005, Japan

subunits. Since the width of the contraction channel was set at a smaller size than the cancer cell, cancer cells underwent squeezing forces in this section, and the center of inertia of these larger cells was aligned along the center of the microchannel. Although the device showed high separation efficiency and separation purity, limitations in throughput and the risk of clogging at the narrow contraction region require improvement. To avoid clogging while maintaining high throughput, we considered developing a microfluidic device to separate cancer cells from blood using only an inertial migration effect.

In a previous study,[28] we investigated the applicability of inertial migration forces to separate cancer cells from a concentrated suspension of RBCs. The experimental results revealed that the inertial migration of cancer cells occurred up to about a 10% Hct condition. Although the developed device was able to collect cancer cells from an RBC suspension, it did not achieve high enrichment of cancer cells. Thus, in the current study, we sought to develop a microfluidic device to separate cancer cells from an RBC suspension with high collection efficiency and enrichment. Although the separation of leukocytes is also important in considering applications to CTC tests, the separation of cancer cells from RBCs should be investigated first, given that RBCs make up most of blood constituents and no former studies have succeeded using only inertial forces.

2. Materials and methods

2.1 Experimental setup

The experimental apparatus consisted primarily of an inverted microscope (IX71, Olympus, Tokyo, Japan) and a high-speed camera (Phantom v7.1; Vision Research, Wayne, NJ). A microchannel was placed on the stage, and the sample was injected using a syringe pump (Fusion 200; Chemyx Inc., Stanford, TX). Images of rigid spheres and cells were taken with the high-speed camera and recorded on a desktop PC.

A schematic of the microchannel is shown in Fig. 1(a). The device had a cascade geometry of stenosed channels and expansions with multiple bifurcations. The height of the channel was 160 μm. The flow rate ratio between the channels leading to the RBC-outlet and cancer-outlet was set at each bifurcation point as follows: approximately 1 : 1 at B1, 1 : 1.2 at B2, 1 : 1.4 at B3, and 1 : 0.5 at B4. The flow ratios were determined so as to lead only RBCs to the RBC-outlet and only cancer cells to the cancer-outlet, which was controlled by adding the appropriate channel resistances.[1] The total flow rate ratio between RBC-outlet and cancer-outlet was about 8.1 : 1.

Fig. 1(b) shows the principle of the separation method used. The microfluidic device uses the inertial migration of cancer cells in the stenosed channels and the increase in the cell-free layer of RBCs at the multiple bifurcations. First, cell-free layers were formed after the first stenosed channel [Fig. 1(b)(i)]. Cancer cells then migrated towards their equilibrium positions after the second stenosed channel [Fig. 1(b)(ii)], where the equilibrium positions existed at approximately $0.6W$ (W: the half width of the channel) away from the channel center.[2] The first bifurcation (B1) split the main flow into two [Fig. 1(b)(iii)], and then cancer cells migrated to their equilibrium position after the third stenosed channel [Fig. 1(b)(iv)]. In this channel, cancer cells migrated towards only one side of the channel, because the

equilibrium position existed $0.6W$ away from the center. At the second bifurcation (B2), an RBC suspension without cancer cells was extracted towards the RBC-outlet and the cell-free layer thickness in the main channel was increased significantly. These successive operations resulted in a reduction in the overlap between cancer cells and RBCs. Finally, cancer cells and RBCs were completely separated at B4 [Fig. 1(b)(v)]; only cancer cells flowed into the cancer-outlet.

The microchannel was fabricated by standard soft lithography with a protocol similar to our previous study.[15] Briefly, a mold for the channel was fabricated on a silicon wafer with a negative photoresist (SU-8 3050; Kayaku MicroChem, Tokyo, Japan). Polydimethylsiloxane (PDMS) (Silpot 184; Dow Corning, Midland, MI) was prepared by mixing the base compound and curing agent at a weight ratio of 10 : 1. After removing bubbles created during mixing, the mixture was poured on the master mold and cured by baking for about 30 min at 90 °C. The PDMS was peeled from the master, and the fluidic ports used as the inlet and the outlets were created with a punch. To prevent fluid leakage from the gap between the PDMS and glass slide, an oxygen plasma treatment was applied to irreversibly bind the PDMS and glass.

2.2 Materials

The poorly differentiated human breast cancer cell line MDA-MB-231 was used for the present study. The average diameter of the cells was about 15 μm. Cells were cultured in a 25 cm² tissue culture flask and maintained in RPMI 1640 (Invitrogen Corp., Carlsbad, CA) with 10% fetal bovine serum (FBS; Thermo Fisher Scientific Inc., Waltham, MA) and 1× antibiotic-antimycotic (Invitrogen) at 37 °C in a humidified atmosphere containing 5% v/v CO_2.[13] In each experiment, cells were grown to 80–90% confluence, and harvested from the tissue culture flasks by adding 0.25% trypsin-EDTA (Invitrogen) and dissociated. The cells were then used in the experiments after washing twice with Dulbecco's phosphate-buffered saline [D-PBS(-)] (Invitrogen).

RBCs were taken from healthy 25- and 26-year-old male and 25-year-old female volunteers and centrifuged to separate the RBCs and other constituents. The RBCs were then preserved in normal saline at 4 °C and resuspended in 5% Dextran 40 (DEX40), in which DEX40 (low density Dextran L 10% w/v in lactated Ringer's solution; Otsuka Pharmaceutical Co. Ltd., Tokyo, Japan) was diluted with the same volume of lactated Ringer's solution (Otsuka Pharmaceutical) prior to each experiment. All procedures were carried out in compliance with the guidelines of the Clinical Investigation Ethics Committee at Tohoku University.

Five types of fluid samples were used:

(a) To observe RBC motion, RBCs alone were suspended in 5% DEX40. The Hct ranged from 0.1% to 10%. The density and viscosity of 5% DEX40 at 25 °C were 1.01×10^3 kg m^{-3} and 1.99×10^{-3} Pa s, respectively.

(b) In rigid sphere collection experiments, only rigid spheres of 15 μm diameter (15 μm Polymer Microsphere Suspension; Thermo Fisher Scientific Inc.) were suspended in 5% DEX40. The concentration of rigid spheres was set at 1×10^4 particles mL^{-1}.
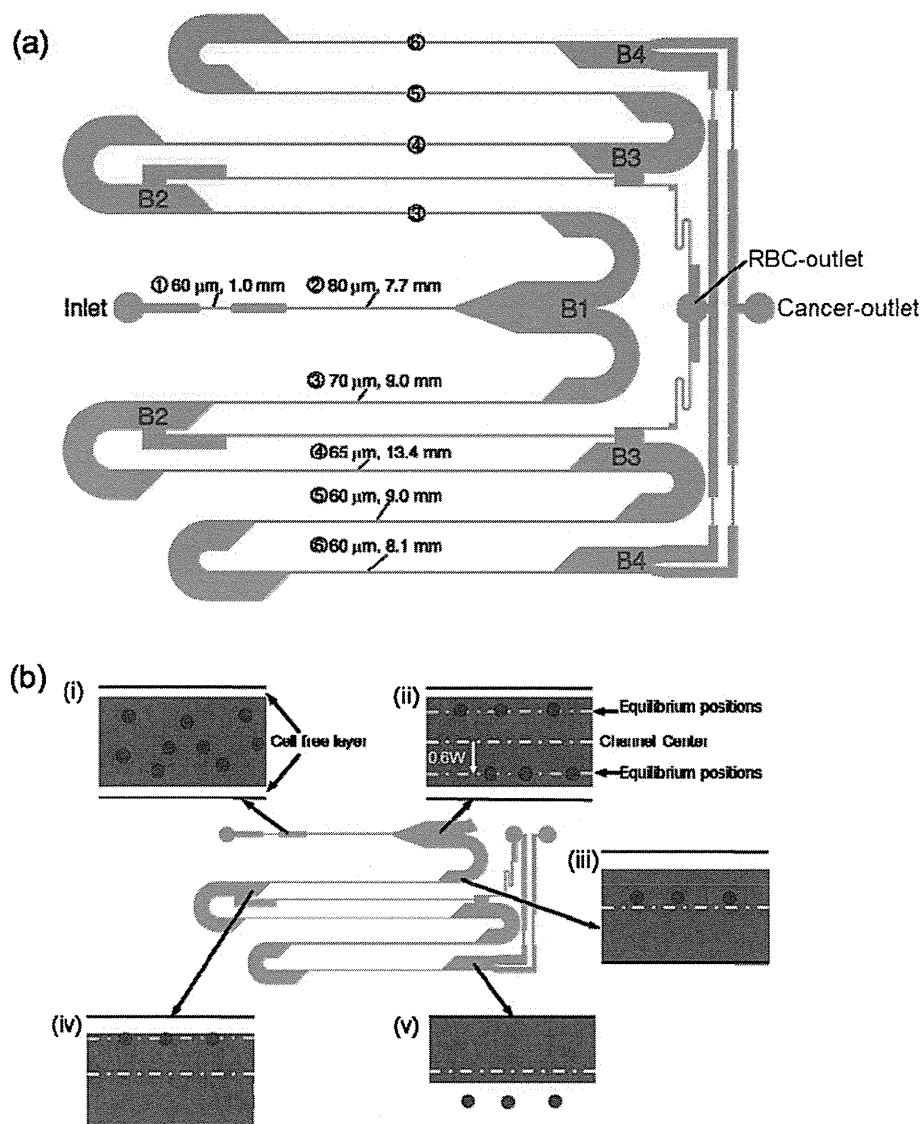
Fig. 1 Schematic of the multistage microchannel system: (a) geometry (width and length) of the device and (b) separation principle of cancer cells from an RBC suspension.

(c) In cancer cell collection experiments, only cancer cells (MDA-MB-231) were suspended in 5% DEX40. The concentration of cancer cells was set at 1×10^4 cells mL^{-1}.

(d) In experiments separating rigid spheres from RBCs, a suspension of 15 µm rigid spheres and RBCs in 5% DEX40 was prepared. The Hct of RBCs was set at 1%, and the ratio of rigid spheres to RBCs was set in the range of 0.03 to 0.1.

(e)In experiments separating cancer cells from RBCs, a suspension of cancer cells and RBCs in 5% DEX40 was prepared. The Hct of RBCs was again set at 1%, and the ratio of cancer cells to RBCs was set in the range of 0.03 to 0.1.

2.3 Experimental procedures

In experiments with fluid (a), a suspension of only RBCs, the total infusion volume was set at 10 mL. Samples were collected from each outlet and the concentration of RBCs in each sample was measured using a cell counter (Vi-CELL XR Cell Viability Analyzer; Beckman Coulter Inc., Brea, CA). We define the

unsuccessful collecting ratio of RBCs from the cancer-outlet, α, as:

$$\alpha = \frac{n_{\text{c-out}}}{\lambda\, n_{\text{R-out}} + n_{\text{c-out}}} \times 100 \ [\%] \qquad (1)$$

where $n_{\text{R-out}}$ is the number density of particles in a sample collected from the RBC-outlet and $n_{\text{c-out}}$ is that from the cancer-outlet. λ is the flow rate ratio between the RBC-outlet and the cancer-outlet, which was 8.1 in this study.

In experiments with fluids (b) and (c), suspensions of only rigid spheres or cancer cells, respectively, particle motion was recorded at bifurcation B4 with a high-speed camera. The images were analyzed and the number of particles flowing into the cancer-outlet or RBC-outlet was counted. The collection efficiency of particles from the cancer-outlet was defined by the ratio of particles flowing into the cancer-outlet to the total particle number. We counted more than 200 particles to calculate the collection efficiency in each experiment.

In experiments with fluids (d) and (e), rigid spheres or cancer cells in an RBC suspension, respectively, it was difficult to observe individual particles and to count the number of particles using image analysis. We therefore used a flow cytometer (JSAN; Bay Bioscience, Hyogo, Japan) to measure the number density of rigid spheres or cancer cells. The number density of rigid spheres in an RBC suspension was counted by measuring the side scatter (SSC) of the particles. To measure the number density of cancer cells in an RBC suspension, cancer cells were labeled with nuclear staining. The labeling protocol was similar to that in our previous study.[28] Briefly, cells were separated from the 5% DEX40 solution by centrifugation. Then, 2 μL of 100-fold diluted DRAQ5 {1,5-bis[(2-(di-methylamino)ethyl) amino]-4, 8-dihydroxyanthracene-9, 10-dione} (Cell Signaling Technology Inc., Danvers, MA) solution was added to the sample, as was 98 μL of PBS, before mixing gently and incubating for 20 min at 4 °C. The sample was washed twice with fresh PBS to remove excess dye. The number density of labeled cancer cells in each sample was determined by measuring the fluorescence intensity of cells. A control test was also performed using non-labeled samples.

The collection efficiency and enrichment of rigid spheres (or cancer cells) were calculated using the following equations:

$$\text{Collection efficiency} = \frac{n_{\text{c-out}} R_{\text{c-out}}}{\lambda\, n_{\text{R-out}} R_{\text{R-out}} + n_{\text{c-out}} R_{\text{c-out}}} \times 100 \quad [\%] \quad (2)$$

$$\text{Enrichment} = \frac{R_{\text{c-out}}}{R_{\text{original}}} \quad (3)$$

where $n_{\text{R-out}}$ is the number density of particles, including rigid spheres (or cancer cells) and RBCs, collected from the RBC-outlet, $n_{\text{c-out}}$ is that from the cancer-outlet, $R_{\text{R-out}}$ is the ratio of rigid spheres (or cancer cells) to RBCs in a sample collected from the RBC-outlet, $R_{\text{c-out}}$ is that in a sample collected from the cancer-outlet, and R_{original} is that in the original sample.

In all of these experiments, the inlet flow rate was set as 565 μL min^{-1}.

3. Results

3.1 Effect of Hct on RBC motion

To achieve high separation purity, it is important to prevent the unsuccessful collection of RBCs from the cancer-outlet. In this section, we use a suspension of only RBCs [fluid (a)] to investigate the effect of Hct on RBC motion. Fig. 2(a) shows the distribution of RBCs at five observation areas under the 1% Hct condition. After the first stenosed channel, a clear cell-free layer developed near the sidewalls. The thickness of the cell-free layer was increased by the repeated bifurcations. Eventually, at the final bifurcation (B4), most of the RBCs were collected from the RBC-outlet.

Samples were collected from the two outlets and the number density of RBCs in each sample was measured. The unsuccessful collecting ratio of RBCs from the cancer-outlet, α, was then calculated using eqn (1). Fig. 2(b) shows the effect of Hct on α. We see that α increased as Hct increased. This is primarily because the thickness of the cell-free layer decreases as Hct is
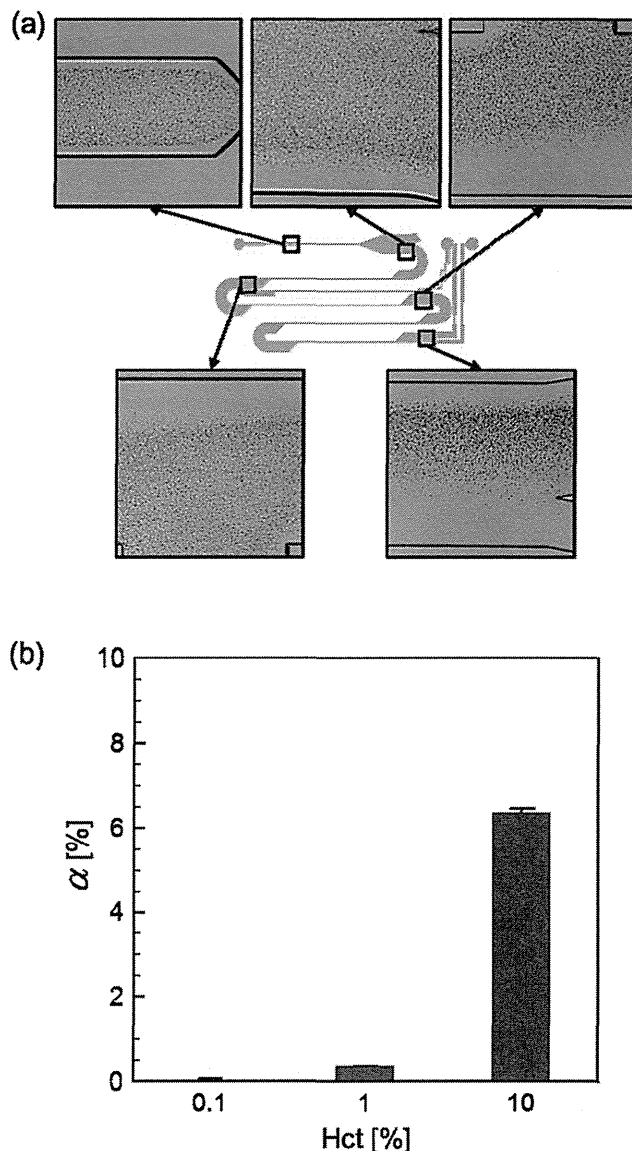

Fig. 2 Effect of hematocrit (Hct) on red blood cell (RBC) motion: (a) distribution of RBCs at five observation areas under a 1% Hct condition; (b) the effect of Hct on α ; error bars indicate the standard deviation.

increased. A similar tendency was also found in our previous study,[10] in which a decrease in the cell-free layer thickness was explained by the diffusion of RBCs due to cell–cell interactions. The results of Fig. 2(b) indicate that the device was able to effectively remove RBCs up to the 1% Hct condition.

3.2 Trajectories of rigid spheres and cancer cells

Next, we investigated the collection efficiency of rigid spheres (15 μm diameter) or cancer cells using a suspension of only rigid spheres or cancer cells [fluid (b) or (c), respectively]. Fig. 3(a) shows the behavior of cancer cells at the four bifurcation areas. At each area, cancer cells were aligned along the same line and most of the cancer cells were collected from the cancer-outlet. The rigid spheres showed similar tendencies to the cancer cells (data not shown).
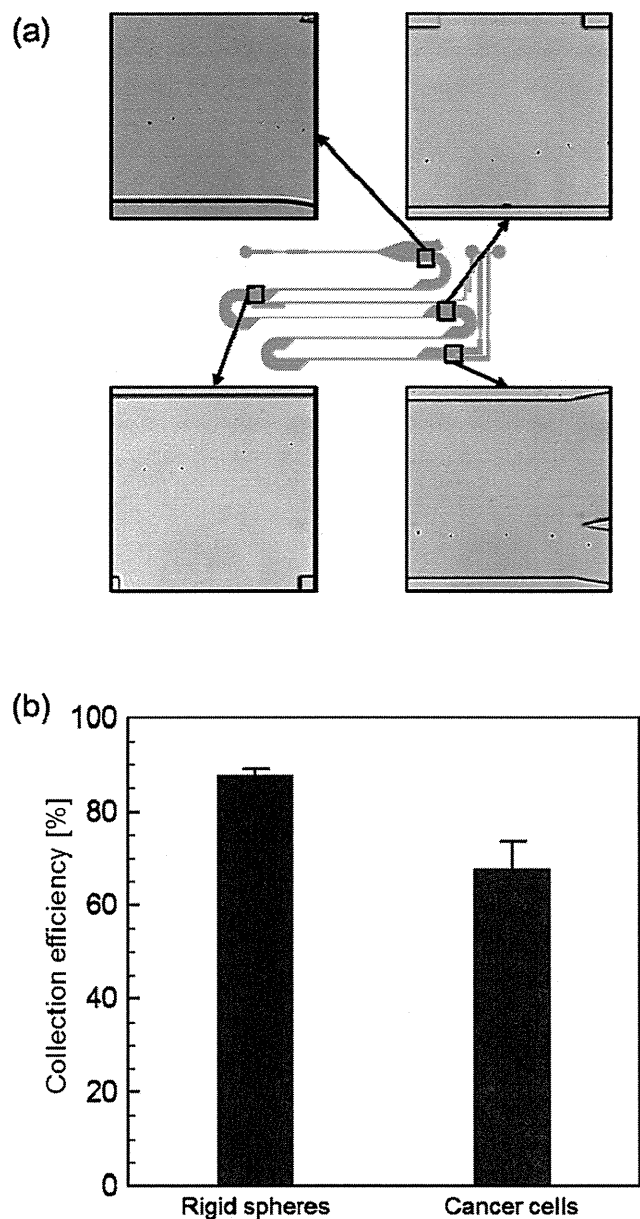
Fig. 3 Separation of rigid spheres and cancer cells: (a) the behavior of cancer cells at four bifurcation areas; (b) collection efficiency of rigid spheres and cancer cells. Error bars indicate the standard deviation.

The collection efficiency of rigid spheres or cancer cells was calculated as explained in section 2.3, and the results are shown in Fig. 3(b). The collection efficiencies of rigid spheres and cancer cells were about 88 ± 2% and 68 ± 6%, respectively. The collection efficiency of cancer cells was lower than that of rigid spheres. This was likely because the cancer cells showed individual differences in size and shape. The size distribution of MDA-MB-231 was reported in our previous study;[28] the average cell diameter was approximately 15 μm, with a standard deviation of about 4.3 μm. Based on previous studies,[19,20,25] equilibrium positions shift towards the channel center as the particle size becomes larger. Thus, in the present study, the equilibrium positions of larger cells shifted towards the channel center, and some of these cells might have flown into the RBC-outlet at bifurcation B2. As a result, some cancer cells were not

collected from the cancer-outlet, and the collection efficiency was decreased as compared with the rigid sphere case. These results indicate that the distribution of cell size is an important factor in separating cancer cells by inertial migration.

3.3 Separation of rigid spheres and cancer cells from an RBC suspension

Finally, the separation of rigid spheres or cancer cells from an RBC suspension was examined using fluids (d) and (e), respectively. The Hct of the RBC suspension was set at 1%, because the unsuccessful collecting ratio of RBCs, α, was small [cf. Fig. 2(b)]. Since the ratio of rigid spheres or cancer cells to RBCs was set in the range of 0.03–0.1%, the two-body interactions between two rigid spheres or two cancer cells would be expected to be negligible.

Fig. 4(a) (bottom-left) shows the behavior of rigid spheres and RBCs at the final bifurcation (B4). Most of the RBCs, shown by gray dots, were collected from the RBC-outlet, while most of the rigid spheres, shown by black dots, were collected from the cancer-outlet. Fig. 4(a) (bottom-right) shows the behavior of cancer cells and RBCs at B4. We again see that most cancer cells, shown by white dots, were collected from the cancer-outlet. These results illustrate that the device could separate rigid spheres and cancer cells from RBCs.

The fluorescence intensities of samples collected from the RBC-outlet and the cancer-outlet were assessed by flow cytometry and the results of a suspension of cancer cells and RBCs [fluid (e)] are shown in Fig. 4(b). The graph is divided into four regions; the lower left region indicates non-labeled cells (i.e., RBCs) and the upper right region indicates labeled cells (i.e., cancer cells). We see that the sample taken from the cancer-outlet had a considerably larger number of cancer cells than that taken from the RBC-outlet.

The channel length required for focusing to equilibrium positions is given by:[7]

$$L_{\mathrm{m}} = \frac{4\pi\mu W^2}{\rho U d^2 f_{\mathrm{L}}} \qquad (4)$$

where μ is the viscosity, ρ is the density, U is the average velocity, d is the particle diameter, and f_{L} is the geometric coefficient. In the first stenosed channel before bifurcation B1, for example, W is 40 μm and f_{L} is 0.05.[7] By assuming that the diameter of cancer cells is 15 μm, L_{m} can be calculated as 4.6mm, which is shorter than the channel length of 7.7 mm. Thus, most of the cancer cells can migrate to the equilibrium positions. RBCs, on the other hand, have diameters of about 8 μm. L_{m} for RBCs is about 16.2 mm, which is longer than the channel length. Thus, most of RBCs may not have enough time to migrate to the equilibrium positions. Eqn (4) can nicely explain the present experimental results.

As explained in section 2.3, the collection efficiency [eqn (2)] can be calculated by the ratio of cancer cells (or rigid spheres) to RBCs as well as the number density of all particles. Fig. 4(c) and (d) show the collection efficiency of rigid spheres and cancer cells, respectively. The collection efficiency of rigid spheres with 1% Hct was about 86 ± 9%, which was not different from that without RBCs (0% Hct). In the case of cancer cells, on the other hand, the collection efficiency with 1% Hct was about 85 ± 7%,
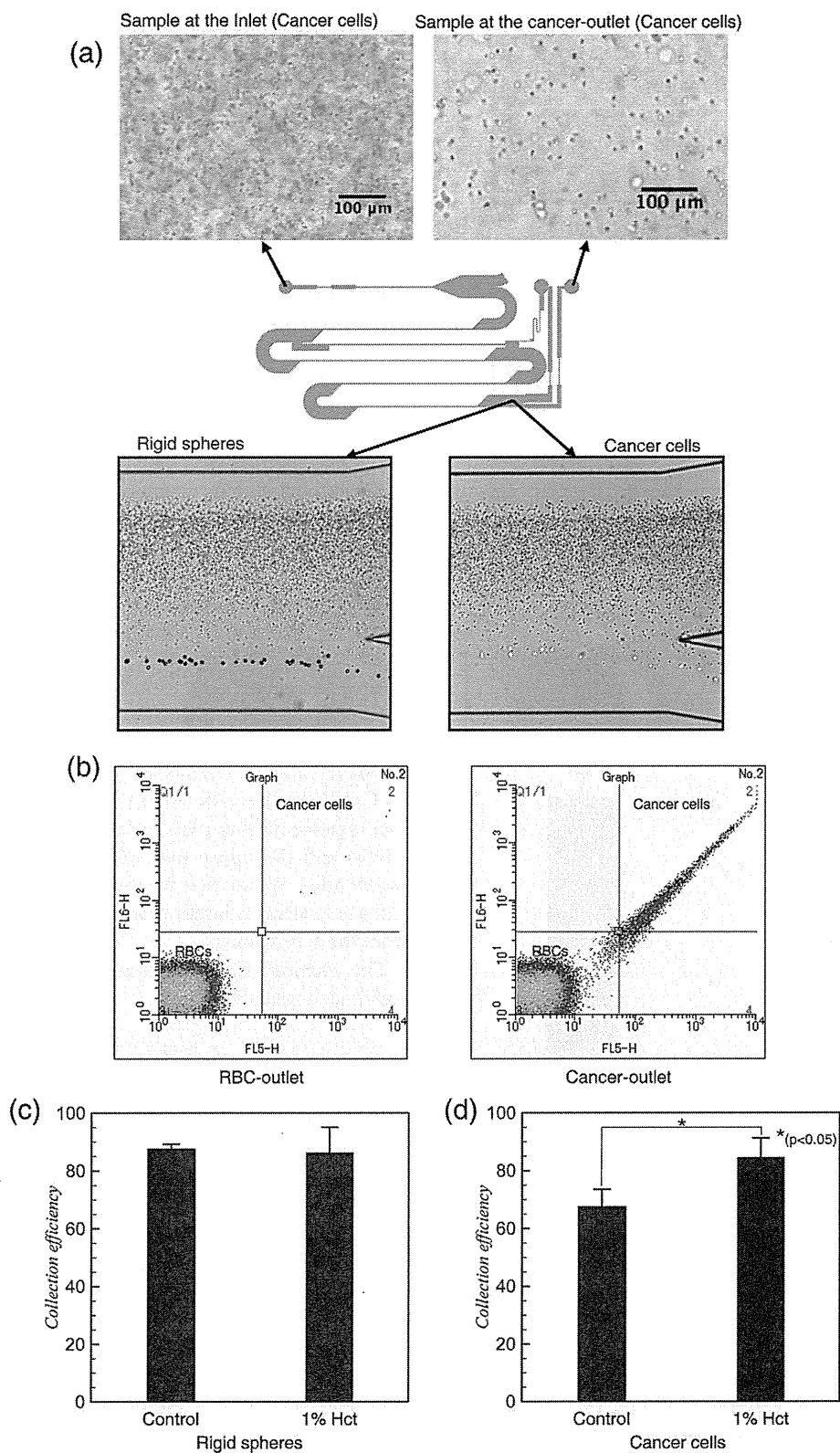
Fig. 4 Separation of cancer cells and rigid spheres from RBCs: (a) a suspension of cancer cells and RBCs at the inlet (top-left), at the final bifurcation B4 (bottom-right), and at the cancer-outlet (top-right). Bottom-left image is a suspension of rigid spheres and RBCs at B4; (b) fluorescence intensity of samples collected from the RBC-outlet and cancer-outlet in the case of a suspension of cancer cells and RBCs; (c, d) the collection efficiency of rigid spheres and cancer cells. The control indicates the collection efficiency without RBCs, and error bars indicate the standard deviation.

which was higher than the collection efficiency without RBCs. This result may seem counterintuitive. When a suspension of RBCs flows in a microchannel, the fluid is strongly mixed by the hydrodynamic interactions between RBCs, as reported in our previous studies.[16,26] Thus, the presence of RBCs likely prevents the inertial migration of cancer cells. On the other hand, cancer cells require a much longer travel distance to show inertial migration as compared with rigid spheres.[28] That is, cancer cells around the center of the channel hardly migrate towards the equilibrium positions. We think that these cells were mixed by the interactions with RBCs and sometimes pushed away from the center. Inertial migration forces acted on these cells, and eventually the cells drifted towards the equilibrium positions. The tendency of increasing collection efficiency with increasing Hct is preferable in achieving high collection efficiency of cancer cells from a RBC suspension.

We should note that the effect of cell–cell interactions cannot be neglected even with a 1% Hct sample, when the microchannel is sufficiently long compared to the width of the channel. This fact can be explained as follows. Let us consider a sphere of diameter d placed in simple shear flow with the shear rate $\dot{\gamma}$. The sphere may interact (or collide) with another sphere, when the center–center distance between the two spheres comes close to about d. The relative velocity of two spheres with the offset of d in the velocity gradient direction is $d\dot{\gamma}$. Thus, the volume V swept out by the sphere in the time period of Δt may be roughly estimated by the product of the cross section, the relative velocity and the time period as $V = \pi d^3 \dot{\gamma} \Delta t$. The volume fraction of spheres c and the number density of spheres n can be correlated as $c = \pi d^3 n/6$. By assuming one collision within Δt, nV has to be unity, which leads to $nV = 6c\dot{\gamma}\Delta t = 1$. When $c = 0.01$, $i.e.$ 1% Hct, the sphere interacts with another sphere in the time scale of $\Delta t = 1/(0.06\dot{\gamma})$. Let a sphere flow with a velocity U in a channel with half-width W and length L. The travel time T of the sphere flowing through the channel is $T = L/U$. The number of collisions N can be given by $N = T/\Delta t$. By assuming $\dot{\gamma} \approx 2U/W$, N can be estimated as $N = 0.12L/W$. In the present study, the stenosed channel before bifurcation B1 has the dimensions: $W = 40$ μm and $L = 7.7$mm [$cf.$ Fig. 2(a)]. By substituting these values, we can estimate that N is about 23. It means that a sphere experiences near-field collisions about 23 times while flowing through the stenosed channel. We thus think that the effect of cell–cell interactions appears considerably even with a 1% Hct sample in our experimental setup.

Lastly, we compare our results with former studies. In the present study, the collection efficiency of cancer cells with 1% Hct was about 85% [$cf.$ eqn (2)]. This value is close to former study done by Bhagat et al.,[3] in which MCF-7 cells were separated by utilizing pinched and inertial migration effects. The enrichment of cancer cells was also calculated by comparing the ratio of cancer cells to RBCs in the original sample and that in a sample collected from the cancer-outlet [$cf.$ eqn (3)]. The enrichment of cancer cells in this study was about 120 ± 40-fold. From Fig. 4(a) (top-left) and (top-right), we also confirm qualitatively that the ratio of cancer cells to RBCs is significantly increased after flowing through the device. By connecting the present device in series, the enrichment can be improved as 120^M, where M is the number of connections. Other popular size-based and immune-mediated CTC sorting techniques typically achieve

10^4–10^6 fold enrichment,[21–23,27,29,31] which corresponds to 2–3 connections of the present device.

The throughput of the device was 565 μL min^{-1}, which is again a similar value to 400 μL min^{-1} reported by Bhagat et al.[3] We think that it is easy to parallelize the present device both two and three dimensionally, given that the device size is small and the channel height is constant throughout the device. By connecting the device in parallel, in series and in lamination layers, we can process a much larger sample volume with much less operation time. These results illustrate that the microfluidic device developed in the present study has the potential to achieve high separation efficiency and significant enrichment of cancer cells.

4. Conclusions

In this study, we developed a multistage microfluidic device to separate cancer cells from an RBC suspension using inertial migration forces. The device was able to effectively remove RBCs up to the 1% Hct condition. It also showed high performance in separating rigid spheres and cancer cells from an RBC suspension with 1% Hct with a throughput of 565 μL min^{-1}. The collection efficiency of cancer cells from an RBC suspension was about 85%, and the enrichment of cancer cells was about 120-fold. Further improvements can be easily achieved by parallelizing the device. These results illustrate that the separation of cancer cells from RBCs is possible using only inertial migration forces, thus paving the way for the development of a novel microfluidic device for future CTC tests.

Acknowledgements

References

1 R. Aoki, M. Yamada and M. Yasuda, In-channel focusing of flowing microparticles utilizing hydrodynamic filtration, *Microfluid. Nanofluid.*, 2009, **6**, 571–576.

2 A. A. S. Bhagat, S. S. Kuntaegowdanahalli and I. Papautsky, Inertial microfluidics for continuous particle filtration and extraction, *Microfluid. Nanofluid.*, 2009, **7**, 217–226.

3 A. A. S. Bhagat, H. W. Hou and L. D. Li, Pinched flow coupled shear-modulated inertial microfluidics for high-throughput rare blood cell separation, *Lab Chip*, 2011, **11**, 1870–1878.

4 G. T. Budd, M. Cristofanilli and M. J. Ellis, Circulating tumor cells *versus* imaging—predicting overall survival in metastatic breast cancer, *Clin. Cancer Res.*, 2006, **12**, 6403–6409.

5 D. D. Carlo, D. Irimia, R. G. Tompkins and M. Toner, Continuous inertial focusing, ordering, and separation of particles in microchannels, *Proc. Natl. Acad. Sci. U. S. A.*, 2007, **104**, 18892–18897.

6 D. D. Carlo, J. F. Edd and D. Irimia, Equilibrium separation and filtration of particles using differential inertial focusing, *Anal. Chem.*, 2008, **80**, 2204–2211.

7 D. D. Carlo, Inertial microfluidics, *Lab Chip*, 2009, **9**, 3038–3046.

8 M. Cristofanilli and G. T. Budd, Circulating Tumor cells, disease progression, and survival in metastatic breast cancer, *N. Engl. J. Med.*, 2004, **351**, 781–791.

9 M. Cristofanilli, D. F. Hayes and G. T. Budd, Circulating Tumor Cells: A novel prognostic factor for newly diagnosed metastatic breast cancer, *J. Clin. Oncol.*, 2005, **23**, 1420–1430.

10 H. Fujiwara, T. Ishikawa and R. Lima, Red blood cell motions in high-hematocrit blood flowing through a stenosed microchannel, *J. Biomech.*, 2009, **42**, 838–843.

11 D. R. Gossett, W. M. Weaver and A. J. Mach, Label-free cell separation and sorting in microfluidic systems, *Anal. Bioanal. Chem.*, 2010, **397**, 3249–3267.

12 S. C. Hur, H. T. K. Tse and D. D. Carlo, Sheathless inertial cell ordering for extreme throughput flow cytometry, *Lab Chip*, 2010, **10**, 274–280.

13 T. Ishikawa and H. Fujiwara, Asymmetry of blood flow and cancer cell adhesion in a microchannel with symmetric bifurcation and confluence, *Biomed. Microdevices*, 2011, **13**, 159–167.

14 S. S. Kuntaegowadanahalli and A. A. S. Bhagat, Inertial microfluidics for continuous particle separation in spiral microchannels, , *Lab Chip*, 2009, **9**, 2973–2980.

15 R. Lima and S. Wada, In vitro blood flow in a rectangular PDMS microchannel: experimental observations using a confocal micro-PIV system, Biomed. , *Biomed. Microdevices*, 2008, **10**, 153–167.

16 R. Lima and T. Ishikawa, Radial dispersion of red blood cells in blood flowing through glass capillaries: The role of hematocrit and geometry, *J. Biomech.*, 2008, **41**, 2188–2196.

17 A. J. Mach and D. D. Carlo, Continuous scalable blood filtration device using inertial microfluidics, , *Biotechnol. Bioeng.*, 2010, **107**, 302–311.

18 J. M. Martel and M. Toner, Inertial focusing dynamics in spiral microchannels, , *Phys. Fluids*, 2012, **24**, 032001.

19 J. P. Matas and J. F. Morris, Inertial migration of rigid spherical particles in Poiseuille flow, , *J. Fluid Mech.*, 2004, **515**, 171–195.

20 J. P. Matas and J. F. Morris, Lateral force on a rigid sphere in large-inertia laminar pipe flow, , *J. Fluid Mech.*, 2009, **621**, 59–67.

21 H. Mohamed, Isolation of tumor cells using size and deformation, , *J. Chromatogr., A*, 2009, **1216**, 8289–8295.

22 S. Nagrath, *et al.*, Isolation of rare circulating tumour cells in cancer patients by microchip technology, , *Nature*, 2007, **450**, 1235–1239.

23 P. Paterlini-Brechot and N. L. Benali, Circulating tumor cells (CTC) detection: Clinical impact and future directions, , *Cancer Lett.*, 2007, **253**, 180–204.

24 E. D. Pratt, C. Huang and B. G. Hawkins, Rare cell capture in microfluidic devices, , *Chem. Eng. Sci.*, 2011, **66**, 1508–1522.

25 G. Segre and A. Silberberg, Behaviour of macroscopic rigid spheres in Poiseuille flow, , *J. Fluid Mech.*, 1962, **14**, 136–157.

26 M. Saadatmand and T. Ishikawa, Fluid particle diffusion through high-hematocrit blood flow within a capillary tube, , *J. Biomech.*, 2011, **44**, 170–175.

27 S. Tan, *et al.*, Microdevice for the isolation and enumeration of cancer cells from blood, , *Biomed. Microdevices*, 2009, **11**, 883–892.

28 T. Tanaka, T. Ishikawa and K. Numayama-Tsuruta, Inertial migration of cancer cells in blood flow in microchannels, , *Biomed. Microdevices*, 2012, **14**, 25–33.

29 G. Vona, Isolation by size of epithelial tumor cells : a new method for the immunomorphological and molecular characterization of circulatingtumor cells, , *Am. J. Pathol.*, 2000, **156**, 57–63.

30 C. Wittekind and M. Neid, Cancer Invasion and Metastasis, , *Oncology*, 2005, **69**, 14–16.

31 S. Zheng, Membrane microfilter device for selective capture, electrolysis and genomic analysis of human circulating tumor cells, , *J. Chromatogr., A*, 2007, **1162**, 154–161.

— 370 —

Properties of *N*-Butyl Cyanoacrylate–iodized Oil Mixtures for Arterial Embolization: In Vitro and In Vivo Experiments

Chiaki Takasawa, MD, PhD, Kazumasa Seiji, MD, PhD,
Kenichi Matsunaga, MD, PhD, Toshio Matsuhashi, MD, PhD,
Makoto Ohta, PhD, Shuya Shida, Kei Takase, MD, PhD, and
Shoki Takahashi, MD, PhD

ABSTRACT

Purpose: To examine the properties of *N*-butyl cyanoacrylate (NBCA) and iodized oil (lipiodol [Lip]) in vitro and in vivo for safe and effective embolization.

Materials and Methods: Viscosity, polymerization time, and diffusing capacity were evaluated according to the NBCA/Lip ratio in vitro. Additionally, the effect of the NBCA/Lip ratio on arterial embolization was evaluated in vivo; various ratios of NBCA/Lip were injected into the renal arteries of adult beagles, after which the embolization effect following transcatheter arterial embolization was quantitatively investigated histopathologically and using computed tomography (CT) volumetry.

Results: The viscosity of NBCA/Lip increased, polymerization time was prolonged, and diffusing capacity increased as the NBCA density decreased. As the NBCA density decreased, embolic material was recognized in smaller diameter arteries, and embolization of a larger vascular bed was accomplished. The NBCA/Lip mixture with a low density of NBCA was located more peripherally from the catheter tip, and embolization of more peripheral and smaller diameter arteries was achieved.

Conclusions: The relationships of properties of NBCA/Lip in vitro and embolization effects in vivo of various ratios of NBCA/Lip were quantitatively examined and compared. The results of this study are useful for safe and effective embolization.

ABBREVIATIONS

Lip = lipiodol, NBCA = *N*-butyl cyanoacrylate

N-butyl cyanoacrylate (NBCA) (Histoacryl; B. Braun Melsungen AG, Melsungen, Germany) is a liquid, permanent embolic material used for transcatheter arterial embolization that polymerizes in the presence of anions. Because the embolization mechanism of NBCA does not depend on

clotting function, it still has a marked embolic effect when clotting function is impaired (1,2). For embolization, NBCA is mixed with iodized oil (Lipiodol [Lip]; Terumo, Tokyo, Japan) in a ratio between 1:1 and 1:9. This mixing is done for two reasons: (*a*) to produce a radiopaque material because NBCA is radiolucent and is not observed on fluoroscopy and (*b*) to adjust the time for polymerization from injection (polymerization time) and the time for completion of embolization by changing the density of NBCA; this allows the material to reach successfully, but not pass through, target blood vessels, possibly with an arteriovenous shunt.

Regarding the mixture ratio, there are two conflicting opinions. One opinion is that the lower the NBCA density, the more peripherally the embolic material reaches because the polymerization time is prolonged. Alternatively, it has been suggested that the lower the NBCA density, the more proximally the embolic material ceases to flow because the viscosity of NBCA/Lip is increased owing to a high Lip density. Clinically, the NBCA/Lip ratio is empirically de-

a.   b.

Figure 1. Digital subtraction angiogram of renal artery obtained before and after embolization. **(a)** Left renal artery angiogram obtained before embolization. **(b)** Left renal artery angiogram obtained after embolization with NBCA-Lip (1:1). The arteries indicated by arrowheads underwent embolization.

cided by a physician performing transcatheter arterial embolization after considering the blood vessel diameter and blood velocity. However, the exact relationship between the NBCA/Lip ratio and intravascular polymerization factors is unknown.

To study intravascular polymerization factors on the side of the embolic material, we evaluated the viscosity, diffusing capacity, and polymerization time of NBCA/Lip according to their ratio in vitro. Additionally, we examined the effect of the NBCA/Lip ratio on arterial embolization in vivo; various ratios of NBCA-Lip were injected into the renal arteries of adult beagles, after which the embolization effect was quantitatively investigated using computed tomography (CT) volumetry and histopathologically. Finally, we assessed how the polymerization time and viscosity of the NBCA/Lip ratio affected arterial embolization.

MATERIALS AND METHODS

This study was approved by the local animal experiment committee.

In Vitro Studies

Viscosity of NBCA/Lip Mixture. The viscosity of the NBCA/Lip mixture was determined using a tuning fork–type viscometer (SV-10; A&D Company, Tokyo, Japan).We measured the viscosity of samples at eight different NBCA/Lip ratios (NBCA:Lip = 1:1 [NBCA density 50%], 1:2 [33%], 1:3 [25%], 1:4 [20%], 1:5 [16.7%], 1:6 [14.3%], 1:7 [12.5%], 1:8 [11.1%], 1:9 [10%]) at a temperature of 37°C.We used Win CT-Viscosity software (A&D Company) to analyze the measurement results.

Diffusing Capacity of NBCA/Lip. When mixed with blood, NBCA/Lip is polymerized to generate a polymer.

The diffusing capacity of NBCA/Lip was evaluated by measuring the area of the generated polymer in blood after its mixing with blood. NBCA/Lip (0.5 mL) was dropped on whole blood (1 mL) from an adult beagle on a Petri dish and shaken with a shaker 100 times per minute. Next, the area of the polymer was measured using Scion image software (National Institutes of Health, Bethesda, Maryland).

Polymerization Time. To determine the polymerization time, NBCA/Lip was dropped on blood, and we recorded the state of polymerization by video (EXILIM EX-FH25; Casio, Tokyo, Japan) at a frame rate of 240 frames/s and observed the morphologic changes in the polymer. The completion of polymerization was defined as the time point when the morphologic changes ceased.

In Vivo Studies

Twelve adult beagles were used for the in vivo experiment (mean body weight, 14.9 kg; range, 13.8–15.8 kg). The dogs were anesthetized with an intramuscular injection of ketamine (40 mg/kg of body weight) and atropine sulfate (0.1 mg). Sodium pentobarbital (Nembutal, 25 mg/kg; Dainippon Sumitomo Pharma, Osaka, Japan) was used as a supplemental anesthetic.

Transcatheter Arterial Embolization. For transcatheter arterial embolization, an 8-F introducer sheath (Medikit, Tokyo, Japan) was inserted into the carotid artery. A baseline angiogram of the abdominal aorta was obtained using a 5-F Cobra catheter (Cook, Inc, Bloomington, Indiana), and then the renal artery was catheterized (**Fig 1**). A 2-F microcatheter (Renegade; Boston Scientific, Natick, Massachusetts) was placed coaxially through the 5-F catheter and positioned distally in the ventral or dorsal branch. Selective embolizations with NBCA/Lip were performed by the same radiologist.
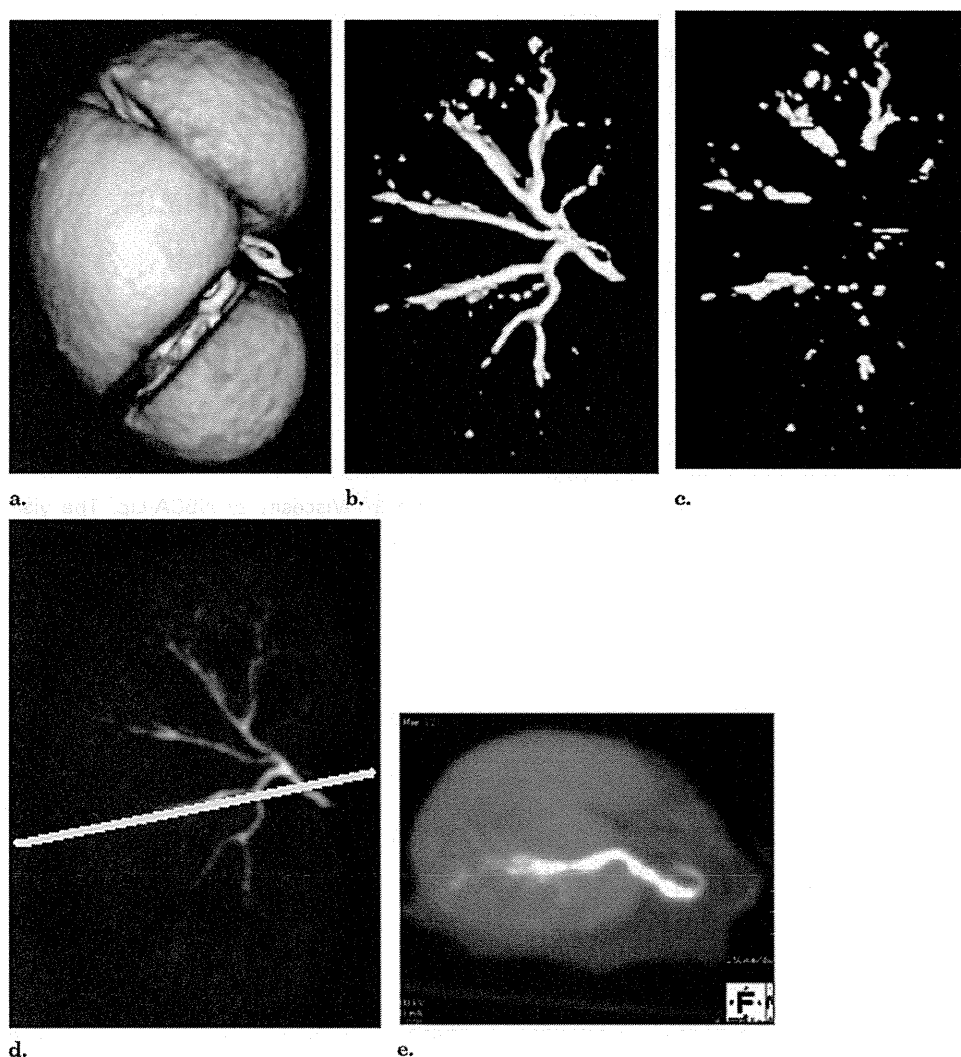
Figure 2. CT volume rendering image and volumetry of the kidney after embolization with NBCA-Lip (1:9). (a) CT volume rendering image of the kidney. (b) CT volume rendering image of the region with a CT value > 500 HU. CT volumetry of this region evaluates the total vascular bed in which the embolic material was distributed. (c) By removing the medullary vessels on source images, volumetry of the vascular bed in which embolization was accomplished only in the cortex was achieved. To consider individual differences in the vascular bed of the kidney, the cortex/total kidney ratio was evaluated. This was considered to be the index of the distal embolization effect. (d) Maximum intensity projection of the kidney. (e) CT axial image of the position of the line on image (d). For pathologic preparation, a region with a high level of NBCA-Lip on CT similar to this was chosen.

The embolization technique was performed as follows: NBCA was mixed with Lip at a ratio of 1:1, 1:3, or 1:9 manually. Before injecting NBCA/Lip, the microcatheter was flushed with 5% dextrose to prevent premature polymerization of the NBCA/Lip triggered by anions from residual blood or saline. NBCA/Lip was injected carefully under fluoroscopic monitoring using a 2.5-mL syringe. Injection speed was decided by the operator to prevent blood stasis. The endpoint of embolization was decided by the operator at the time of flow arrest of NBCA/Lip at fluoroscopy.

Immediately after injection, the microcatheter was retracted to prevent the catheter tip from adhering to the vessel wall. Next, the inner lumen of the guiding catheter was aspirated, and the contralateral embolization procedure was performed using a new microcatheter. The injected volume was measured by subtracting microcatheter luminal volume (0.67 mL) from the injected volume. Embolization was performed in eight kidneys using each NBCA/Lip ratio.

CT Volumetry. Immediately after embolization, the dog was killed with an overdose of sodium pentobarbital; exsanguination was performed, and the kidneys were removed. A CT scan of the specimen was obtained, and the intravascular distribution of Lip was confirmed using 64-slice multidetector CT (Aquilion 64; Toshiba, Tokyo, Japan). Using CT volume-rendering images of the kidney with a threshold CT value > 500 HU, CT volumetry of the vascular bed after embolization was performed at a workstation (Ziostation version 1.3.0.2.; AMIN, Inc, Tokyo, Japan) (**Fig 2**). We measured the volume of cortical vessels

that underwent embolization after removing the medullary vessels on source images and evaluated the vascular bed in which embolization was achieved only in the periphery, not including the medullary part of the kidney. For the index of the distal embolization effect, we did not use the absolute value of the cortical vessels that underwent embolization but rather the ratio of vessels of the cortex that underwent embolization and those of the entire kidney (V-cortex/V-kidney) to exclude the variation effect of different volumes of the renovascular bed among different subjects.

Histopathologic Evaluation. The specimen was fixed in 10% neutral buffered formalin solution for 1 to 2 weeks and then was subjected to alcohol dehydration. Additionally, a region with a high level of NBCA/Lip on CT was chosen for pathologic preparation. This tissue was embedded in paraffin and stained with hematoxylin and eosin and Elastica-Masson. After a preliminary experiment of renal artery embolization with NBCA alone, NBCA/Lip, and Lip alone, embolic material was pathologically identified as amorphous structures that stained with either hematoxylin and eosin or Elastica-Masson within vessels that underwent embolization; these amorphous structures were never seen in control vessels that did not undergo embolization.

In each kidney, 40 random fields were observed at 400× magnification. A histopathologic evaluation determined the following two points to evaluate how far the NBCA/Lip traveled in the artery: (*a*) point 1, the smallest minor axis of the arteriole containing embolic material in the lumen was measured in each kidney; (*b*) point 2, the number of arterioles with a minor axis ≤ 40 μm containing embolic material in the lumen was counted. A sampling error secondary to specimen preparation may affect point 1, so point 2 was used as another index of the distal embolism effect, which could be regarded as quantitative evaluation of the distal embolism effect.

Statistical Analysis

Statistical analysis was performed using the SPSS software package (version 15.0; SPSS Inc, Chicago, Illinois). Histopathologic evaluations were compared using analysis of variance (ANOVA) with the Tukey-Kramer post hoc test. A P value < .05 was considered statistically significant.
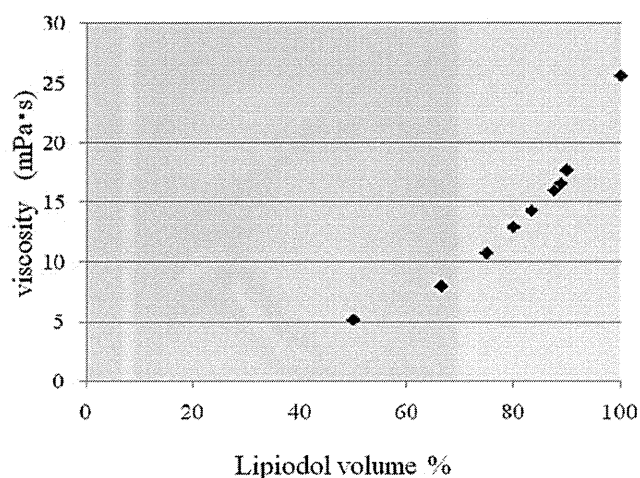
RESULTS

In Vitro Studies

With the increased amount of Lip, both the viscosity of NBCA/Lip and the area of the polymer increased (**Figs 3** and **4**). The polymerization time also increased with the Lip volume (**Fig 5**).

In Vivo Studies

Transcatheter arterial embolization of the renal artery succeeded in all cases. On average, 0.43 mL (range, 0.3–0.6

**Figure 3.** Viscosity of NBCA-Lip. The viscosity of NBCA-Lip increased exponentially with the volume of Lip.
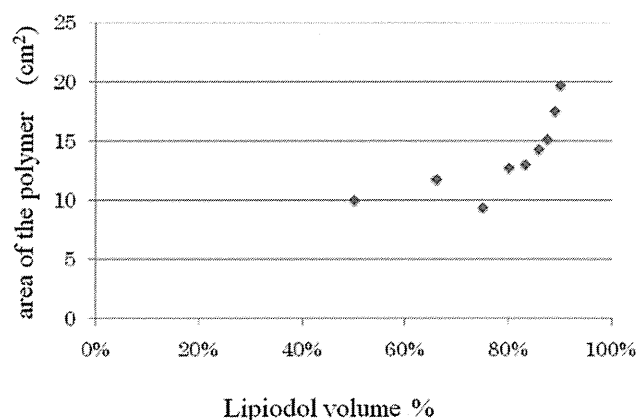
Figure 4. Diffusing capacity of NBCA-Lip. As an index of the diffusing capacity of the NBCA-Lip polymer in blood, we measured the area of the polymer on a Petri dish. The area of the polymer increased exponentially with the volume of Lip.
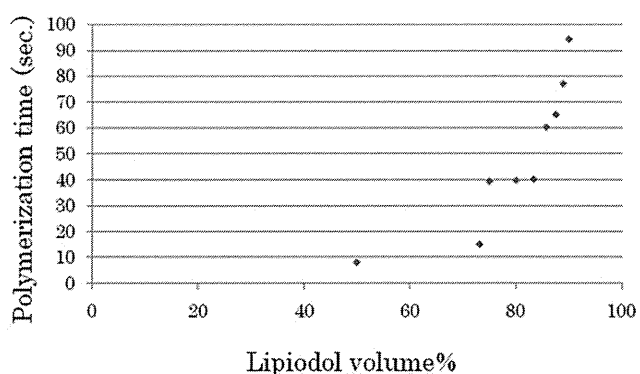
Figure 5. Polymerization time of NBCA-Lip. The polymerization time increased with the Lip volume. The time was similar between ratios 1:1 and 1:2 and between ratios 1:3 and 1:5 and increased exponentially in ratios 1:6–1:9.

mL) of NBCA/Lip was required to achieve embolization in all kidneys. No significant difference was noted in the quantity injected among the three groups.
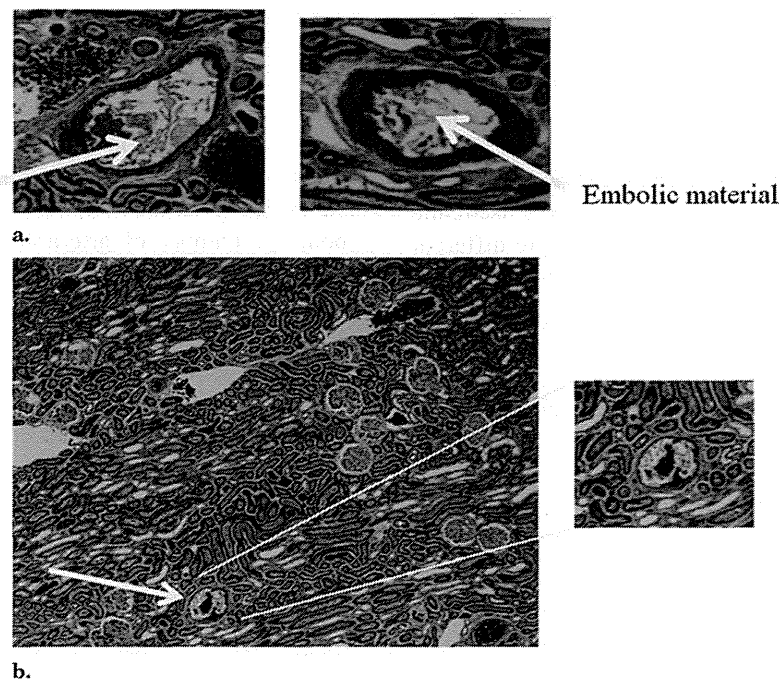
Figure 6. Photomicrograph of renal medulla obtained immediately after embolization with NBCA-Lip. (Elastica-Masson; original magnification, ×400.) **(a)** Section of arteriole of renal medulla. The amorphous material in the artery is embolic material. **(b)** The smallest minor axis of the arteriole containing embolic material in the lumen was measured in each kidney.

The cortical vascular bed in which embolization was achieved increased as the Lip volume increased. The cortical vascular bed in which embolization was achieved was significantly greater with NBCA/Lip ratios of 1:3 and 1:9 than with NBCA/Lip ratio of 1:1; no significant difference was observed between NBCA/Lip ratios of 1:3 and 1:9 (**Fig E1** [available online at www.jvir.org]).

Regarding evaluation point 1 (**Fig 6** and **Fig E2** [available online at www.jvir.org]), the minimum minor axis of an arteriole that contained embolic material in the lumen was 3.4 μm, 2.2 μm, and 2.3 μm with NBCA/Lip ratios of 1:1, 1:3, and 1:9. With ratios of 1:3 and 1:9, the embolic material was found in significantly narrower arterioles than with a ratio of 1:1.

Regarding evaluation point 2 (**Fig E3** [available online at www.jvir.org]), the average number of arterioles in which embolization was accomplished in 40 fields was 1.1, 5.6, and 6.3 with ratios of 1:1, 1:3, and 1:9. At a low NBCA density, embolization was achieved in narrow arterioles, and the peripheral distribution of the embolic material tended to be wider. Embolization was achieved in more arterioles at a 1:9 ratio than at a 1:1 ratio; no significant difference was found between 1:1 and 1:3 ratios and between 1:3 and 1:9 ratios.

DISCUSSION

When performing transcatheter arterial embolization, reaching as close to the target as possible with embolization of only the target artery is critical. When embolization occurs prematurely or much proximal to the target, only a temporary embolization effect may result because recanalization via collateral circulation would develop. Embolization immediately proximal to the target (ie, distal embolization) is needed to obtain a permanent embolization effect on the target. However, selective insertion of the microcatheter is often difficult because of increased tortuosity or small size of the target artery. When some distance consequently remains between the microcatheter tip and the target, distal embolization that would be desirable may become unachievable.

Little is known regarding the polymerization time of NBCA/Lip after injection, and a risk exists of excessive or incomplete embolization or adhesion of the catheter tip to the vascular wall. The ratio is empirically decided by an interventional radiologist considering the blood vessel diameter, blood velocity, and distance from the microcatheter tip to the target. Successful embolization has been reported at the following ratios for different target arteries: bronchial artery, 1:7 (3); gastrointestinal organs, 1:1–1:7; splenic artery, 1:3–1:4; lower dorsal branch of the renal artery, 1:4 (2); lumbar artery, 1:1; inferior epigastric artery, 1:7; and iliac artery, 1:5. However, the optimal ratio may not be constant for each artery and may differ in different cases depending on circumstances such as the blood vessel diameter, blood velocity, and distance from the microcatheter tip to the target.

Experimental examination of the embolization effect of NBCA has been reported. Performing embolization of rat renal arteries with different ratios of NBCA/Lip (1:1